

High Temperature Oxidation of Nickel-Based Cermet Coatings Composed of Al_2O_3 and TiO_2 Nanosized Particles

M. A. Farrokhzad · T. I. Khan

Received: 28 July 2013 / Revised: 30 September 2013 / Published online: 11 October 2013
© Springer Science+Business Media New York 2013

Abstract The use of co-electrodeposited nickel-based cermet coatings has been recently considered as a low cost method for protecting the surface of mechanical equipment and machinery against corrosion and high temperature oxidation that are being used in a new oil extraction techniques known as the in situ combustion (ISC) process. In the ISC process, the presence of high temperature atmospheric air can degrade the surface of commercially alloyed components rapidly. This paper investigates the high-temperature oxidation behaviour of novel nanostructured cermet coatings composed of two types of dispersed nanosized ceramic particles (Al_2O_3 and TiO_2) in a nickel matrix and produced by co-electrodeposition technique. For this purpose, high temperature oxidation tests were conducted in dry air for 96 h at 500, 600 and 700 °C to obtain the mass changed per unit of area at specific time intervals. Statistical techniques as described in ASTM G16 were used to formulate the oxidation mass change as a function of time. The cross-section and surface of the oxidized coatings were examined for both visual and chemical analyses using wavelength dispersive X-ray spectroscopy element mapping, X-ray diffraction and energy-dispersive X-ray spectroscopy. The results showed sub-parabolic oxidation behavior up to 600 °C and quasi-linear at temperatures between 600 and 700 °C for the coatings. The spectroscopy results showed formation of two Ni–Ti–O compounds (Ni_3TiO_5 and NiTiO_3) between the dispersed TiO_2 and nickel that can ultimately reduce the oxidation rate for the coatings.

Keywords Co-electrodeposition · Nanostructured coatings · Cermet · High temperature oxidation · NiTiO_3 · Ni_3TiO_5

M. A. Farrokhzad (✉) · T. I. Khan
The University of Calgary, 2500 University Drive NW, Calgary, AB, Canada
e-mail: mafarrok@ucalgary.ca

Introduction

In a new oil extraction technique known as the in situ combustion (ISC) process, temperatures as high as 700 °C are utilized to reduce the viscosity of bitumen products for an easier extraction from the reservoir [1]. In these environments, the presence of high temperature atmospheric air can rapidly degrade the surface of commercially alloyed components. At high temperatures, almost all engineered alloys react chemically with gases and as a result of the oxidation process, some degree of surface degradation can be expected for the exposed mechanical components to these aggressive environments. To protect the surface of alloyed components against rapid oxidation reactions, it is economically feasible to cover them with coating materials that have lower oxidation rates compared to the alloyed components. In recent years, there has been an increasing demand for using low cost surface protective coating materials against high temperature oxidation in oil extraction and production applications and therefore, use of ceramic-metallic (cermet) coating materials have been suggested. Research has shown that cermet coatings have improved corrosion and high temperature oxidation resistances when they are exposed to gaseous environments at elevated temperatures compared to pure form of metals and alloys [2, 3].

For most metals when they exposed to a high temperature gas, the oxidation rate is defined as an increase in thickness (or mass per unit of area) of the oxide layer as a function of time. Since the oxide layer growth during oxidation is of a diffusion process in nature, the oxidation rate can be defined by linear, logarithmic or parabolic equations [4]. One theory that has been proven to be more accurate and can be applied to a vast majority of metals is Wagner's theory of oxidation that has been developed based on Fick's first law for diffusion [5–7]:

$$\frac{dx}{dt} = -D \frac{\partial C}{\partial x} \quad (1)$$

where x and t are the oxide thickness and time variables, D is the diffusion coefficient and C is the concentration of transferred charged particles. Wagner's theory provides a parabolic rate equation in which the oxide film growth rate for pure metals is controlled by diffusion of charged particles (electrons, cations and ions) crossing the oxide film layer [5–8]. Based on these assumptions, Fick's first law of diffusion can be used to formulate the growth rate of the oxide layer through a diffusion process. Therefore the answer to Fick's law for most metals which defines the growth rate of the oxide layer can be simplified to [9]:

$$x^2 = k't \quad (2)$$

where k' is the parabolic rate of oxidation constant when measuring the oxide film thickness. Equation 2 can also be written based on measurement of mass change per unit of area (m/A):

$$\left(\frac{\Delta m}{A}\right)^2 = k''t \quad (3)$$

where k'' is the parabolic rate of oxidation constant when measuring mass change per unit of area during the oxidation. Meanwhile recent developments in oxidation

of electrodeposited composite coating has shown that the oxidation kinetics can be described by a modified version of Eq. 3 [10, 11]:

$$\frac{\Delta m}{A} = kt^a + C \quad (4)$$

where k is called oxidation rate constant, a , is called growth time constant and C is a general constant of integration. Research has shown that nanostructured cermet coatings composed of a metallic matrix with incorporated ceramic particles can be used as a protective layer to reduce the rate of surface degradations caused by oxidation and therefore, an increase in life of components can be expected. Nickel-based nanostructured cermet coatings produced by co-electrodeposition of nano-sized ceramic particles (such as Al_2O_3 or TiO_2) into a nickel matrix have shown promising results in the past but so far, little research has been conducted to characterize their functionality. Nickel-based cermet coatings composed of only Al_2O_3 have shown significant increase in hardness and therefore they are used for improving the erosion resistance in heavy machinery exposed to erosive environments [12–15]. On the other hand, nickel-based cermet coatings containing TiO_2 have shown lesser degrees of improvement in hardness but they are better known for their improved thermal stability against high temperature oxidation [16]. To our best knowledge, there has been no study on the oxidation performance of nickel-based cermet coatings when both Al_2O_3 and TiO_2 particles are incorporated in the matrix. However, based on the research conducted on cermet coatings composed of only one type of Al_2O_3 or TiO_2 particles, it is believed that nickel-based cermet coatings with both TiO_2 and Al_2O_3 can potentially have the benefits of improved thermal stability from dispersion of TiO_2 particles and the improved mechanical properties from dispersion of Al_2O_3 particles.

Previously the high temperature oxidation behaviour of nickel-based cermet coatings composed of either Al_2O_3 or TiO_2 particles at 500 and 700 °C was characterized by the authors of this paper [17]. This paper focuses on the study of performance of nickel-based cermet coatings when both Al_2O_3 and TiO_2 particles are incorporated in the nickel matrix and oxidized at 500, 600 and 700 °C. The hardness of the coatings developed for this research was also previously analyzed and two electrolyte solution compositions (named A1 and B1) were found to provide an optimal mechanical properties [18]. For an analysis on high temperature oxidation performance of the selected coatings in this research, specimens of A1 and B1 coatings produced by co-electrodeposition on carbon steel substrate were oxidized in dry air for 96 h at 500, 600 and 700 °C and the mass change per unit of area for each type coating was measured at the given specific time intervals. Method of least square and t -distribution [19, 20] was used for statistical analysis and obtaining confidence intervals of the results and also formulating the oxidation mass changes based on Eq. 4. Based on the results, the oxidation rate (k) and growth time (a) constants for each test condition were obtained. The oxidation rate (k) and growth time (a) constants were used to compare the performance of coatings under similar test conditions. In addition SEM micrographs, EDS chemical analysis and WDS element mapping of the coatings were used for further analysis of the coating performance and progression of the oxide layer. The XRD analysis was also used

for analysis of phase and compound formations as a result of oxidation reactions between the oxygen and constituents of the cermet coatings.

Experimental Procedures

Materials

This study used two types of nanosized ceramic powders; alumina (α -Al₂O₃) and titania (TiO₂) purchased from M K Impex Corp. Ltd. The purity for α -Al₂O₃ powder was 99.95 % (with traces of Na: 300 ppm, Si: 3.5 ppm, Ca: 1.6 ppm, Fe: 0.2 ppm, and Co: 0.8 ppm). The purity for TiO₂ powder was 98 % (with traces of Al: 20 ppm, Ca: 75 ppm, Mg: 65 ppm, Nb: 119 ppm, S: 165 ppm and Si: 102 ppm). The average grain size (measured using TEM) was 20 nm for Al₂O₃ and 50 nm for TiO₂ particles. The substrate material was made from a hot-rolled AISI-1018 carbon steel sheet and the specimens for co-electrodeposition were cut in a rectangular shape (length: 25 mm, width: 12.5 mm and thickness: 4 mm). The mill scale was removed by mechanical cleaning and the surface was prepared to a 600 grit SiC finish. The specimens were then cleaned in alkaline solutions (E-Kleen 102-ETM and E-Kleen 129-LTM) and finally an acid pickling solution (with 31 % HCl) was used to remove any remaining grease or contaminants from the surfaces of the substrate specimens prior to the co-electrodeposition of the coatings.

Co-Electrodeposition of Cermet Coatings

The standard Watt's bath formula was used for the chemical composition of the electrolyte solution and the concentrations of ceramic particles in the electrolyte solution were obtained from previous research [12, 17, 18, 21]. The pH of the electrolyte solutions was measured to be 4.0–4.2 and the temperature was kept between 50 and 55 °C. The electrolyte solutions were composed of two mixtures of ceramic powders, which were called A1 and B1. The coatings classification and the compositions of the electrolyte bath solutions are summarized in Table 1.

The anode was cut from a high purity (99.9 %) nickel bar. The coatings were produced using a standard DC setup for electroplating. A current density of 2 A/dm² was applied for 60 min for the electrodeposition of the coatings. Scanning electron microscopy (JEOL JXA-8200) was used to measure the average electrodeposited coating thickness. The produced average thickness was measured to be 40 ± 5 μm. The particle contents in the nickel matrix for each type of coatings were measured using the “Image J” software program. The process of converting SEM images into black and white binary images has been described in detail by Parida et al. [22]. The measurement of volume fraction for Al₂O₃ and TiO₂ particles in the nickel matrix were calculated and are provided in Table 1. The results showed that the volume fraction for each type of dispersed particle in the nickel matrix did correspond proportionally to its molar concentration in the electrolyte bath.

Table 1 Type and concentration of electrolyte solutions, electrodeposition parameters and dispersed particle counts in nickel matrix

Coatings	Molar concentration	Particles in electrolyte (mass%)	Stirring speed	Electrolyte composition	Applied current density and time	Particle contents (vol.%)
A1	Al ₂ O ₃ : 0.25 M TiO ₂ : 0.25 M	Al ₂ O ₃ : 25.5 g/l TiO ₂ : 20 g/l	350 rpm	Standard <i>Warr</i> 's bath solution: nickel sulphate hexahydrate (1 M), nickel chloride hexahydrate (0.2 M), and boric acid (0.5 M), dissolved in distilled water	2 A/dm ² applied for 1 h electrodeposition time	Al ₂ O ₃ : 5.3 % ± 0.5 % TiO ₂ : 5.5 % ± 0.4 % Total: 10.8 vol.%
B1	Al ₂ O ₃ : 0.375 M TiO ₂ : 0.125 M	Al ₂ O ₃ : 38.25 g/l TiO ₂ : 10 g/l	380 rpm			Al ₂ O ₃ : 6.8 % ± 0.4 % TiO ₂ : 2.4 % ± 0.6 % Total: 9.2 vol.%

Oxidation Tests

Oxidation tests were performed using an electric tube furnace (*CARBOLITE-Eurotherm 2416CG*) equipped with an automated temperature control system. The relative humidity (RH) of air is defined by ASHRAE (American Society of Heating, Refrigerating and Air-Conditioning Engineers) standards and is adjusted by the air conditioning system used in the lab. The relative humidity of a lab is usually set for human comfort (which is between 50 and 60 % RH but also subject to hourly climate changes) and it was believed that this level for relative humidity of the work place where oxidation tests were conducted could affect the experiment results. Therefore, the air used for the experiment was received from a laboratory-scale compressed air distribution system, which uses compression to remove the humidity from the air. With the air compressed, partial pressure of the water vapour in the air can increase to the point where moisture can be condensed out of the air at a higher temperature and therefore when released in the electric oven, it is relatively dry. The measured humidity for the compressed air was below 1 %, which is considered extremely dry by ASHREA air conditioning standards. The coated specimens were placed into a quartz tube and then into the center of the furnace. The temperature for the oxidation tests were 500, 600 and 700 °C. For each type of coating three specimens were co-electrodeposited and oxidized in the tube furnace for the given times and temperatures. Three specimens were used for producing mass change diagrams as a function of time. The weight of the specimens before and after oxidation tests was measured using an electric balance with an accuracy of 0.1 mg. Two of these specimens were later cold mounted and used for metallographic, SEM and WDS element mapping analysis. The remaining specimen was used for XRD analysis. Table 2 provides the high temperature oxidation parameters applied in this research.

Microstructural Characterization

For the grain size analysis of the powders a *Tecani F20-200 kV* (the Netherlands) transmission electron microscope (TEM) in bright-field (BF) mode was used. A *JSM-8200 JEOL* micro-probe (Tokyo, Japan) scanning electron microscopy (SEM) in the back-scattered electron mode (BSE) was used for the images of the cross-sections and energy dispersive spectroscopy (EDS) of chemical analysis of selected areas. The element maps were produced using the wavelength dispersive spectroscopy (WDS) of the same *JSM-8200 JEOL* micro-probe. A Rigaku Multiflex X-ray diffractometer (Japan) was used for the X-ray diffraction spectroscopy (XRD) of oxidized specimens.

Statistical Analysis Methods

An effective way of analyzing data for oxidation mass change experiments was to plot all measured data on a logarithmic scale (also known as log–log linear plot). By applying this method both oxidation rate constant (k) and growth-rate time constant (a) can be calculated and thus an oxidation formula can be written in a linear

Table 2 High temperature oxidation tests parameters

Oxidation specimen	Temperature (°C)	Time (h)	Specimen quantity
A1	500	6, 12, 24, 48, 72 and 96	3 specimens for each type of coatings and time interval
B1	600		
	700		

algebraic equation format ($y = mx + b$). This method is known as curve fitting or least square line method. Needless to say, an increase in the number of specimens in any experiment can increase the level of statistical accuracy; however the number of specimen tested in an experiment is usually limited by factors such as equipment limitations, duration of each test and number of parameters studied. A reasonably small population of specimens can be used for an experiment if there is a periodic measurement of specimens in place by considering the standard deviation of all measurements rather than for a single exposure period. Although it is true that by reducing the sample population, the confidence level of the experiment can be affected, however the confidence limits of measurements can be calculated and applied to the interpretation of results. Based on some preliminary pilot oxidation tests which were done during the early stages of this research, it was calculated that a sample population of 3 specimens when mass change is measured at least 6 times, can produced reliable results with a confidence limit over 90 %. It was also calculated that this number of measurements could produce a sufficient amount of data for statistical analysis and measuring the mean and the standard deviation values. For all experiments, the confidence limit for each parameter was measured using the following formula:

$$\Delta = \pm \frac{t^* \times S}{\sqrt{n}} \quad (5)$$

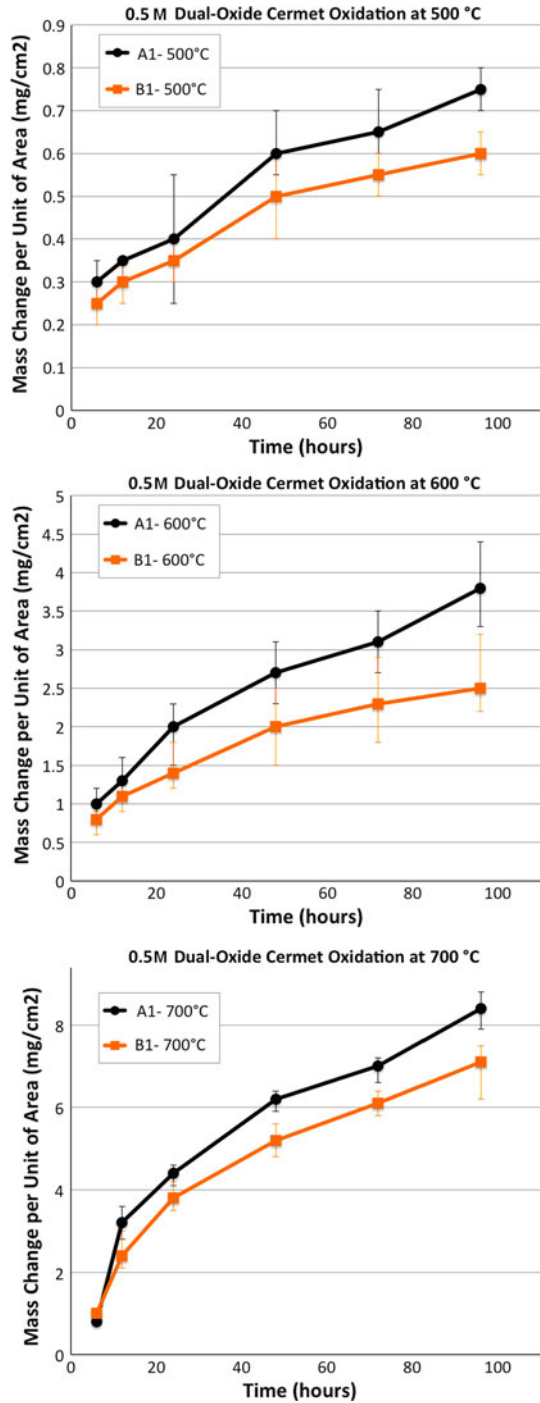
where Δ is the limit that included the true mean value, t^* is the t -distribution, S is calculated standard deviation for each test and n is the sample population. The value for t^* (or t -distribution) can be calculated or obtained from statistical tables. Also for 3 specimens for each test parameter, the degree of freedom (DOF) is equal to 2 ($DOF = n - 1$ or $3 - 1 = 2$). The details of these statistical analyses are extensively provided in ASTM G16—Standard Guide for Applying Statistics to Analysis of Corrosion Data [19].

Results

Oxidation Mass Change Results

The mass change per unit of area results for A1 and B1 coatings oxidized at 500, 600 and 700 °C in dry air are illustrated in Fig. 1. The corresponding logarithmic plots of the mass change results were calculated and presented in Fig. 2. The individual measurements for each test conditions are also included on logarithmic

Fig. 1 The *graphs* show the mass change per unit of area as a function of time for A1 and B1 coatings oxidized at 500, 600 and 700 °C



graphs (Fig. 2) with respect to the calculated standard deviations and two confidence intervals of 68 % ($\pm 1S$) and 95 % ($\pm 2S$).

SEM Images of the Oxidized Coatings

Figure 3 represents the BSE-SEM of the cross-sections of oxidized A1 and B1 specimens oxidized in dry air at 500, 600 and 700 °C for different time intervals up to 96 h. The images were taken of oxidized specimen at time intervals of 6 and 96 h at 500 °C and time intervals of 6, 24, 48 and 96 h for specimens oxidized at 600 and 700 °C. Formation of adherent oxide films on the surface of the coatings can be seen in these images.

Element Maps

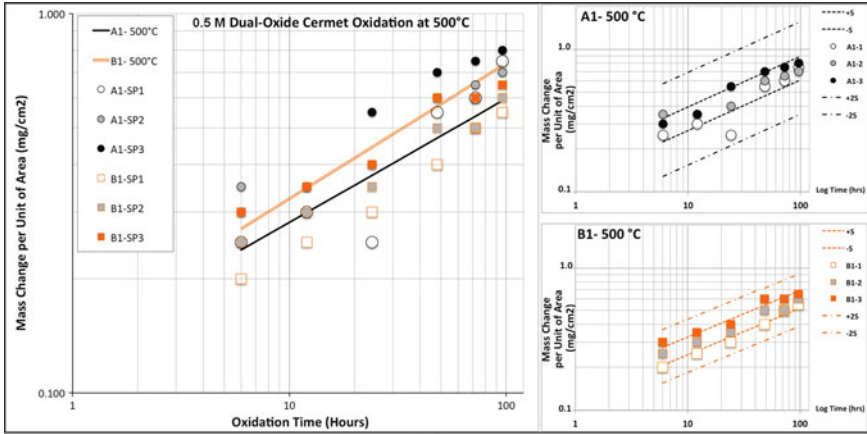
Figure 4 represents the element distribution maps for aluminum (Al) and titanium (Ti). The element maps were produced by microprobe WDS area-scans from the surfaces of oxidized A1 and B1 coatings oxidized at 500, 600 and 700 °C and after 96 h of oxidation in dry air. The element map analysis of the non-oxidized coating surface was also included for comparison. For easier comparison between A1 and B1 coatings, the elements maps were put in pairs.

The colour scale for the element maps displays the local X-ray intensity (measured as [counts/ $\mu\text{A ms}$]) at the given locations. The X-ray intensity of each element can be correlated to relative concentration (mass%) of the selected elements on the maps. The conversion of X-ray intensity of an element to its relative mass% concentration (C') can be done using Castaing's approximation [$C' \approx (I_{SP}/I_{ST}) \times C_{ST}$] where I_{SP} and I_{ST} are the intensity measured from the specimen and the standard sample respectively, and C_{ST} is the concentration of the element in a known standard sample. The values for the intensity (I_{ST}) and concentration (C_{ST}) for the standard sample can be obtained from a known pure form of the element. It should be emphasized that the measured values for the relative mass% concentration of each element in the map should be considered as an approximation because a variety of other parameters such as spectrometer arrangement, age of spectrometer filament, beam intensity and so on can affect the accuracy of the measured X-ray intensity.

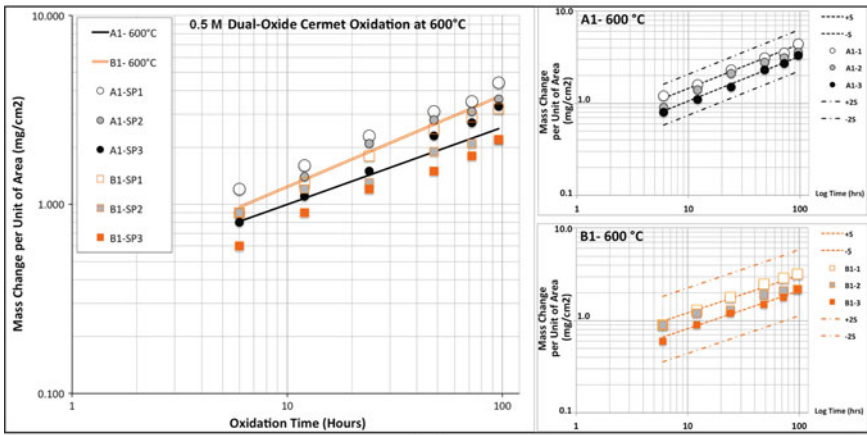
The large colour spots on the aluminum map (compared to the titanium maps) correspond to large colonies of clustered alumina (Al_2O_3) particles. Although the average size of the as-received powder form of Al_2O_3 particles was around 20 nm, some of the Al_2O_3 particles tend to form clusters when they are added into Watt's electrolyte solution and consequently when they are deposited in the nickel matrix, they form large colonies. As a result, large particles (compared to dispersion of TiO_2 particles) were detected in the element maps for aluminum for this research.

XRD Analysis

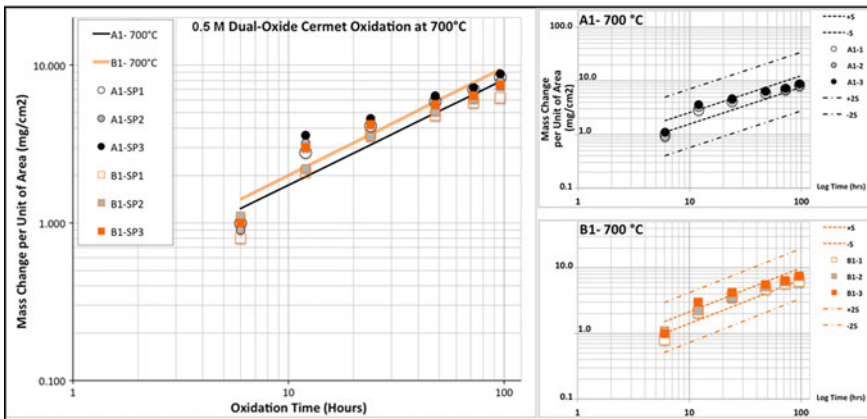
Figure 5 represents the XRD analyses from the surfaces of A1 and B1 coatings oxidized for 96 h at 500, 600 and 700 °C. The matching angles for the elements and



(a)



(b)



(c)

◀ **Fig. 2** Logarithmic oxidation mass change (log–log plots) as a function of time for A1 and B1 coatings oxidized at 500 °C (a), 600 °C (b) and 700 °C (c)—standard deviations of individual measurements from log–log plots represent the variation from the mean value $\pm 1S$ (68 % confidence interval) and $\pm 2S$ (95 % confidence interval) are shown next to each plot

compounds of the coatings constituents were identified and shown on the graphs. The XRD analyses of the oxidized surfaces for both A1 and B1 at all three temperatures did not find any significant compound of aluminum on the oxidized surfaces. Meanwhile, the XRD results showed formation of two Ni–Ti–O compounds; NiTiO₃ (perovskite) and Ni₃TiO₅.

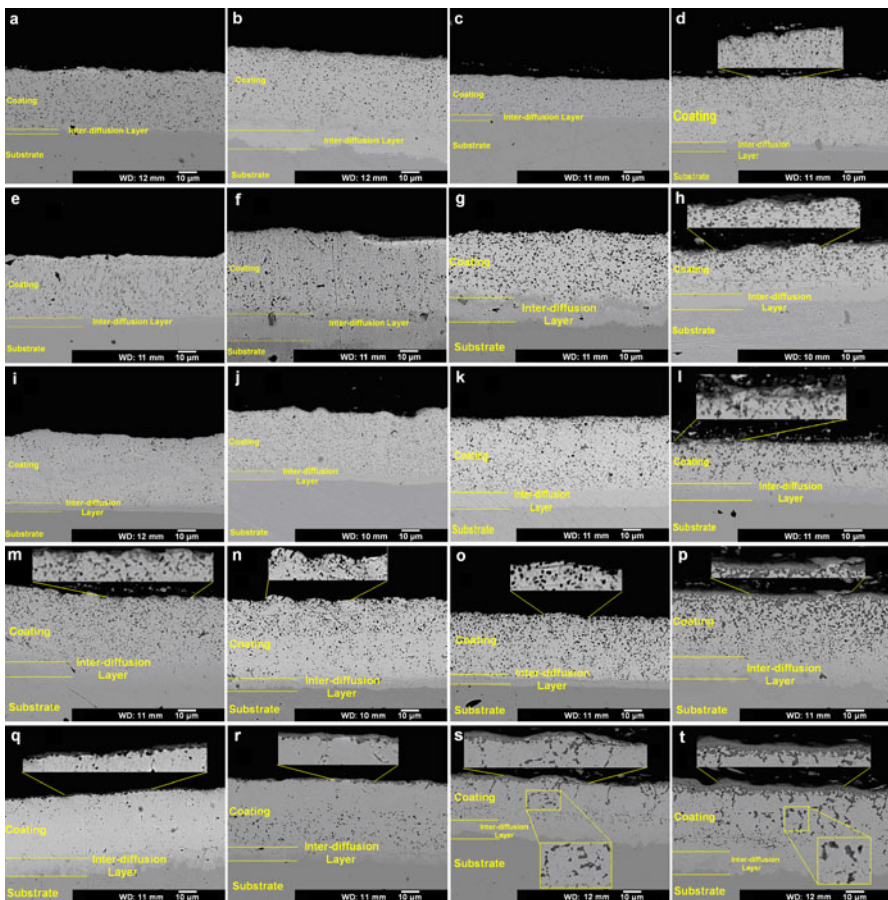


Fig. 3 *First row:* SEM images of A1 and B1 coatings at 500 °C; **a** A1 after 6 and **b** after 96 h, **c** B1 after 6 h and **d** after 96 h. *Second row:* A1 at 600 °C after; **e** 6, **f** 24, **g** 48 and **h** 96 h. *Third row:* B1 at 600 °C after; **i** 6, **j** 24, **k** 48 and **l** 96 h. *Fourth row:* A1 at 700 °C after; **m** 6, **n** 24, **o** 48 and **p** 96 h. *Fifth row:* B1 at 700 °C after; **q** 6, **r** 24, **s** 48 and **t** 96 h

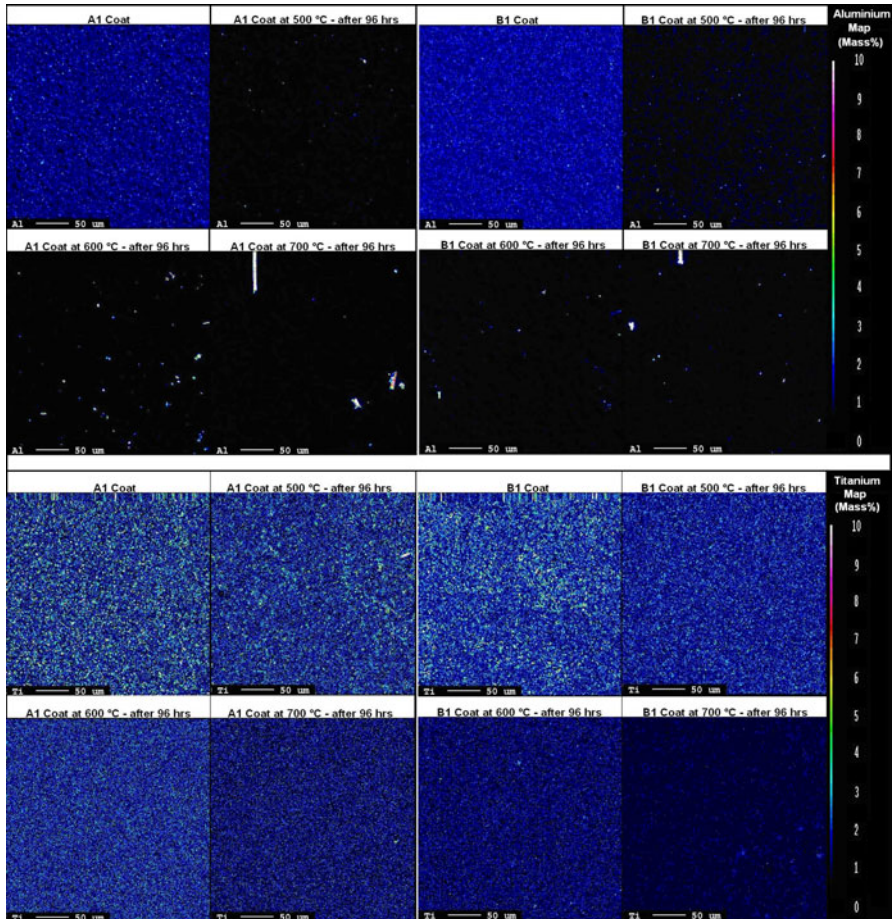


Fig. 4 Aluminum and titanium map for A1 and B1 coatings after 96 h oxidation: non-oxidized coating (*top-left*), at 500 °C (*top-right*), at 600 °C (*bottom-left*) and at 700 °C (*bottom-right*)

Discussion

Oxidation Mass Change Results (Study of Temperature)

The calculated confidence limits for Figs. 1 and 2 representing the oxidation mass change per unit of area for A1 and B1 coatings at 500, 600 and 700 °C are listed in Table 3.

The confidence limits showed a reliable limit for all the tests with a range between 90 and 99.5 %. In addition confidence intervals of 68 % ($\pm 1S$) and 95 % ($\pm 2S$) were also plotted for each experiment (see Fig. 2) showing that the spread of measured data is close to mean value for all the coatings. To study the extent of these differences between the coatings, the statistical method of curve fitting—least

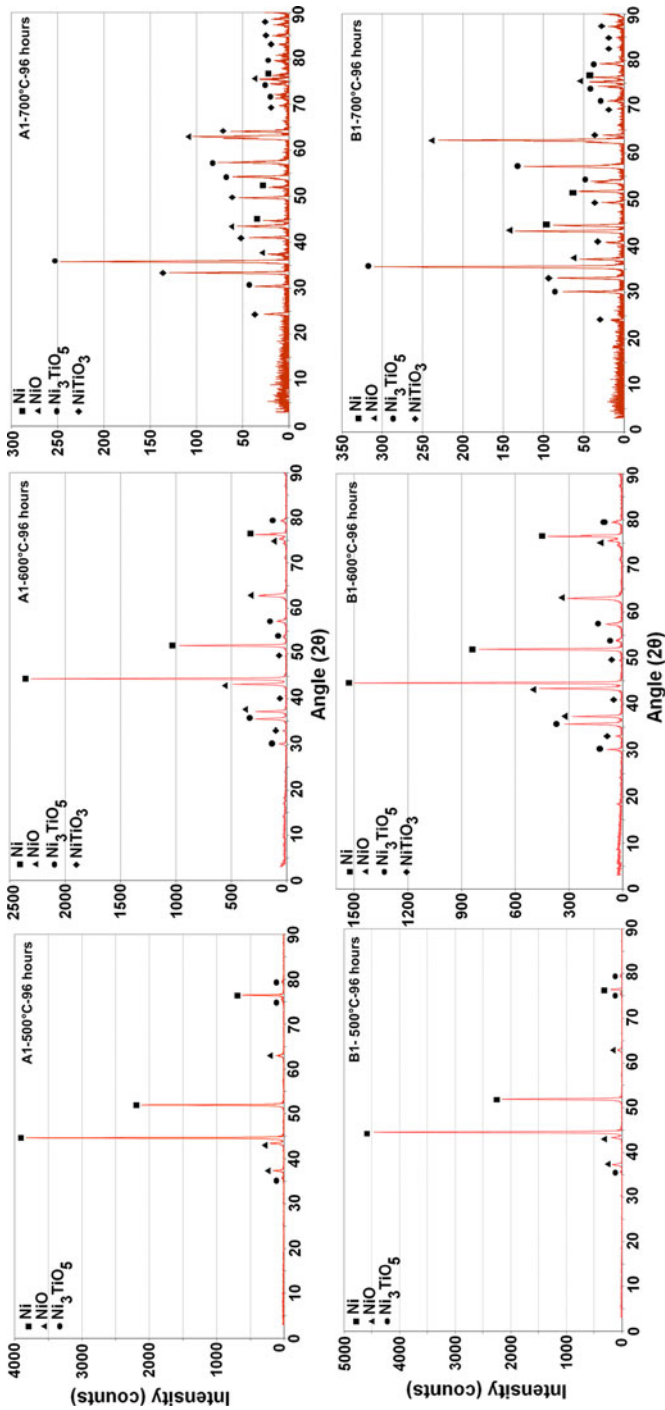


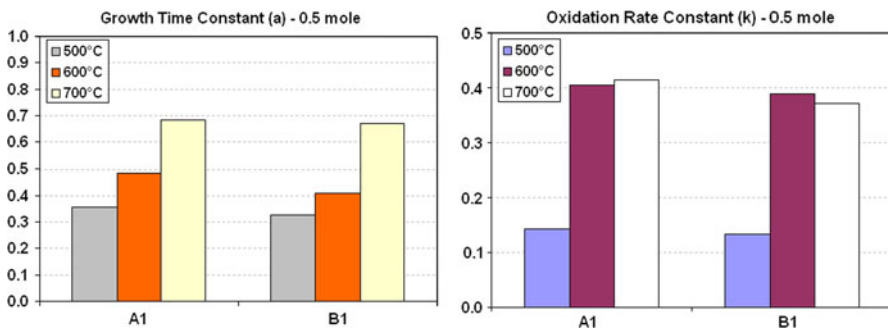
Fig. 5 XRD analyses for A1 and B1 coatings oxidized for 96 h at: **a** 500, **b** 600 and **c** 700 °C

Table 3 Mass change confidence limits for double-component oxides coatings-oxidation tests

Coating	Temp. (°C)	<i>n</i>	Calculated Δ	Calculated <i>S</i>	Calculated <i>t</i>	Confidence limit (CL) %
A1	500	3	0.15	0.082	3.168	95 % < CL < 97.5 %
B1	500	3	0.1	0.062	2.794	90 % < CL < 95 %
A1	600	3	0.6	0.068	15.283	CL > 99.5 %
B1	600	3	0.7	0.086	14.098	CL > 99.5 %
A1	700	3	0.5	0.107	8.094	99 % < CL < 99.5 %
B1	700	3	0.9	0.09	17.321	CL > 99.5 %

Table 4 Calculated oxidation rate and growth time constants for A1 and B1 (0.5 M): 500, 600 and 700 °C

Coating type (Temperature)	$m = a$	$b = \log(k)$	<i>k</i>	On logarithmic plot $y = mx + b$	$f(t) = \frac{\Delta m}{A} = kt^a$
A1 (500 °C)	0.35695	-0.84451	0.14305	$y = 0.35695x - 0.84451$	$f(t) = 0.14305 \times t^{0.35695}$
B1 (500 °C)	0.32646	-0.87625	0.13297	$y = 0.32646x - 0.87625$	$f(t) = 0.13297 \times t^{0.32646}$
A1 (600 °C)	0.48512	-0.39295	0.40462	$y = 0.48512x - 0.39295$	$f(t) = 0.40462 \times t^{0.48512}$
B1 (600 °C)	0.40941	-0.41069	0.38843	$y = 0.40941x - 0.41069$	$f(t) = 0.38843 \times t^{0.40941}$
A1 (700 °C)	0.68466	-0.38342	0.41360	$y = 0.68466x - 0.38342$	$f(t) = 0.41360 \times t^{0.68466}$
B1 (700 °C)	0.67026	-0.43083	0.37083	$y = 0.67026x - 0.43083$	$f(t) = 0.37083 \times t^{0.67026}$

**Fig. 6** Comparison between oxidation rate constant (*k*) and growth time constant (*a*) for A1 and B1 at 500, 600 and 700 °C

square was applied on the results and algorithmic plots of the results were obtained for all three temperatures. From these graphs both oxidation rate constant (*k*) and growth-rate time constant (*a*) for each coating was calculated and the results are listed in Table 4. Additionally, Fig. 6 graphically illustrates and compares the calculated *a* and *k* values for A1 and B1 coatings.

Growth-Rate Time Constants (a)

The growth-rate time constant (a) for both A1 and B1 coatings increased when the oxidation temperature was increased. However the differences between the two coatings for any given temperature remains insignificant with B1 coating showing slightly lower growth-rate values compared to the A1 coating. In addition both A1 and B1 coatings showed sub-parabolic oxidation rates for 500 and 600 °C. It can also be concluded that for 700 °C a quasi-linear growth-time rate can be expected for the coatings.

Oxidation Rate Constants (k)

The oxidation rate constants (k) for both A1 and B1 coatings were increased when the temperature was increased from 500 to 600 °C. However between 600 and 700 °C, this value did not change noticeably for A1 and in fact it was slightly lowered for B1 coatings. The oxidation rate constant (k) is a temperature-dependent parameter and follows Arrhenius equation [7]:

$$k = k_0 \exp \frac{-Q}{RT} \quad (6)$$

where k_0 is a constant related to oxide composition and gas pressure, Q is the activation energy for oxide growth, R is the universal gas constant and T is the temperature in Kelvin. Therefore, it was expected that k constant would increase when temperature was increased from 600 to 700 °C. One possible explanation for this unexpected difference in oxidation rate constants (k) could be found when the k value is written for outward diffusion of nickel cations (or equally inward diffusion of oxygen ions) in Nernst-Einstein equation format [7]:

$$k = \frac{-1}{RT} \int_{\mu_M^i}^{\mu_M^0} D_c d\mu_M = \frac{1}{RT} \int_{\mu_A^i}^{\mu_A^0} D_a d\mu_A \quad (7)$$

where D_c is diffusivity coefficient for Ni cations, μ is the chemical potential gradient, μ_M^i is chemical potential gradient for metal cations (nickel) at the metal-oxide interface and μ_M^0 is the chemical potential for nickel cations at the oxide-gas interface. Similarly, μ_A^i is the chemical potential for oxygen ions at the gas-oxide interface and μ_A^0 is the chemical potential for oxygen ions at the oxide-metal interface. Once the oxide films are completely formed and are adherent to the surface of the coating, the inward diffusion oxygen ions from the oxide layer to the oxide-metal interface will be reduced (hence a smaller D_a) and consequently this will reduce the outward diffusion of nickel cations from the metal matrix into the oxide layer. In other words, once an adherent oxide layer is formed on the surface of the nickel matrix, both inward diffusion of oxygen ions and outward diffusion of nickel cations are reduced and therefore a smaller value for the oxidation rate (k) can be expected.

It should be noted that based on data from Table 4 and Fig. 6, both A1 and B1 coatings showed similar behavior when oxidized in air at 500, 600 and 700 °C. However, the oxidation rates for B1 coatings were slightly lower compared to A1 coatings. This was unexpected because A1 coatings consist of a greater quantity

(see Table 1) of TiO_2 (5.5 %) compared to the TiO_2 content for B1 coating (2.4 %). Based on the results published previously on the oxidation tests cermet coatings containing only one type of Al_2O_3 or TiO_2 particles, coatings with dispersed TiO_2 in the nickel matrix showed lower oxidation rate compared to coatings with dispersed Al_2O_3 in a nickel matrix [16, 17]. However it should be noted that the difference in the amount of mass change measurements between A1 and B1 coatings is not significantly different from each other for the given temperatures. For instance, the mass change difference between A1 and B1 coatings after 96 h of oxidation at 700 °C (Fig. 1) is approximately 1 mg/cm^2 and this difference can be under the influence of other factors such as localized internal oxidation of iron diffusing from the substrate into the nickel matrix.

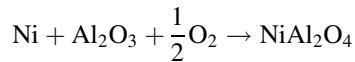
Analysis of SEM Images from Oxidized Coatings

SEM images from the oxidized A1 and B1 coatings did not show a significant difference between the microstructural features of the two coatings oxidized at 500 °C after 6 and 96 h of oxidation (see Fig. 3). At this temperature, the oxide film thickness on the surface of the coating remains relatively thin and below the SEM magnifying capacity. For the specimens oxidized at 600 °C and after 96 h, a relatively thicker oxide layer has grown (between 1 and 2 μm) on the surface. In addition, some darker spots started to appear in the depth of the coating matrix after 96 h of oxidation. The EDS analysis showed that they were rich in oxygen and nickel (possibly NiO). Meanwhile, the microstructural features of the oxidized coating at 700 °C is significantly different when compared to SEM images of coatings oxidized at 500 and 600 °C. The oxide layer on the surface is thicker (2–3 μm) and the size and quantity of the darker spots in the depth of the matrix also increased when the temperature was increased to 700 °C. The EDS analysis of these spots showed that they were rich in oxygen, nickel and iron (Fe) which suggested that some localized internal oxidation of iron from the substrate can have taken place in these spots which is a result of migration (diffusion) of iron cations from the steel substrate into these spots and then oxidized with excessive diffusing oxygen ions from the surface. It should be noted that cracks were not found on the surface of the A1 and B1 coatings at all tested temperatures, which suggest an adherent oxide film formation on the surface.

Analysis of Element Maps and XRD Results

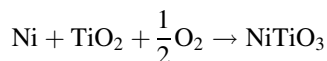
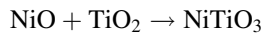
The element mapping analysis was conducted on the oxidized surfaces of A1 and B1 coatings to study the effects of inward diffusion of oxygen ions into the nickel matrix and outward diffusion of nickel and their effects on dispersed Al_2O_3 and TiO_2 particles into the matrix. Images shown in Fig. 4 represent the titanium and aluminum maps for the coatings. The maps also show the original coating element scans and oxidized specimens oxidized for 96 h at 500, 600 and 700 °C. Aluminum maps revealed a rather interesting feature of a reduction in the quantity of aluminum content (from Al_2O_3 particles) when the temperature of oxidation was increased. For both coatings the dispersion frequency and concentration of aluminum was

drastically reduced as temperature was increased. The XRD analysis of the surface of the coating did not show any Ni–Al–O compounds at any temperatures. Phillips et al. [23] and Rhamdhani et al. [24] have studied the phase formation between Ni, O and Al₂O₃ and they have concluded that the only intermediate ternary compound present in Ni, NiO, Al₂O₃ (corundum) phase diagram is NiAl₂O₄ (nickel aluminate) which can form based on the following chemical reaction:



Trumble and Rühle [25] have also concluded that nickel aluminate can only form at temperatures above 650 °C. However, The XRD results did not find the formation of nickel aluminate on the surface of the coatings. Therefore, the reduction in quantity of aluminum on the element maps was believed to be the result of outward diffusion of nickel ions to the surface and the fact that they did not form any nickel aluminum (Ni–Al) s as they bypassed the dispersed Al₂O₃ particles.

Unlike Al₂O₃ particles, the XRD results showed that the dispersed TiO₂ particles in the nickel matrix formed at least two Ni–Ti–O compounds; NiTiO₃ (pervoskite) and Ni₃TiO₅. At 500 °C, only one type of Ni–Ti–O compounds (Ni₃TiO₅) was identified on the oxidized surface of the coatings. At 600 and 700 °C, both compounds were present in the oxidized surface of A1 and B1 coatings. The intermediate ternary compound between Ni, NiO and TiO₂ (anatase) is NiTiO₃ (nickel titanate). Literature review showed that nickel titanate NiTiO₃ can be formed in the presence of NiO and TiO₂ at around 600 °C [26, 27]. NiTiO₃ is the only stable compound between Ni, NiO and TiO₂ [16] that also can co-exist and form joined structures with TiO₂ particles [28]. Formation of NiTiO₃ can take place from the following reactions [29]:



Both of these reactions can take place on the surface of the A1 and B1 coatings during the oxidation with air. Ni₃TiO₅ was found in the XRD result which is a compound that can be found in meta-stable phases at low temperatures similar to the temperature applied in this research but can also become a stable phase at much higher temperatures [30, 31].

The titanium maps of the surface of oxidized coatings at all three temperatures showed that titanium exists on the oxidized coating surfaces which can be from both TiO₂ particles or Ni₃TiO₅ and NiTiO₃ compounds. For the A1 coating that has a higher TiO₂ content (5.3 %) the change in the quantity and frequency of Ti in the coating remains relatively unchanged for all three temperatures. The titanium map for the B1 coating showed that the presence of titanium in the oxidized surface of the coating was reduced when the temperature was increased. The reduction in titanium for the B1 coating can be attributed to the lower titanium oxide content (2.4 %) and higher Al₂O₃ content (6.8 %) in the matrix as compared to the A1 coating and the fact that Al₂O₃ does not form compounds with nickel. Zeng et al. [16] have argued that formation of the NiTiO₃ may contribute to the lower oxidation

rates for the alloys, especially at temperatures below 750 °C. The formation of Ni–Ti–O compounds in the oxide layer can have an impact on the oxidation rate of cermet coatings in two ways; (1) some of the diffusing oxygen ions can potentially be captured and stored in the compound structures (Ni_3TiO_5 and NiTiO_3) which result in a lower diffusion rate of oxygen ions towards the bulk of the nickel matrix and consequently; (2) it can cause a reduction in the rate of outward diffusion of nickel towards the metal-oxide interlayer. It also should be noted that, the XRD analyses did not find any Fe–Al–O or Fe–Ti–O binary or ternary compounds on the surface of the oxidized coatings. One explanation for not finding any of these oxides is that a sufficient amount of Fe for formation of these compounds did not reach the surface, however, internal oxidation of iron within the nickel matrix can make the formation of Fe–Al–O or Fe–Ti–O compounds possible.

Conclusions

High temperature oxidation tests for the cermet coatings produced by co-electrodeposition and composed of both Al_2O_3 and TiO_2 nanosized particles into a nickel matrix were conducted in dry air for 96 h at 500, 600 and 700 °C and the mass changed per unit of area at 6 specific time intervals were obtained for each sample. The method least square line was used for curve fitting analysis to calculate oxidation rate constant (k) and growth time constant (a) with reliable statistical confidence levels between 90 and 99.5 %. The oxidation rate formulas also were calculated based on a method provided by other researchers, most notably Susan and Marder [10, 11]. The results showed sub-parabolic oxidation behavior up to 600 °C and quasi-linear at temperatures between 600 and 700 °C for the coatings. XRD results showed formation of two Ni–Ti–O compounds (Ni_3TiO_5 and NiTiO_3) between the dispersed TiO_2 and nickel, however XRD results did not find formation of Ni–Al–O compounds at any temperatures. Element maps showed a reduction in the quantity of aluminum in element maps which was correlated to the effects of outward diffusion of nickel cations bypassing Al_2O_3 particles without chemically reacting with them. The element maps also showed a relative stability in quantity of titanium on the surface of oxidized coatings which was correlated to formation of Ti–Ni–O compounds. It was concluded that the formation of Ni–Ti–O compounds in the oxide layer can reduce the oxidation rate of cermet coatings by capturing some inward diffusing oxygen ions which can also directly reduce the rate of outward diffusing nickel cations.

Acknowledgments The authors would like to thank the department of Mechanical and Manufacturing Engineering University of Calgary, Alberta, Canada and NSERC Canada, and Statoil Canada Ltd. for their financial support.

References

1. L. M. Castanier and W. E. Brigham, *Journal of Petroleum Science and Engineering* **39**, 125–136 (2003).
2. Q. Feng, T. Li, H. Teng, X. Zhang, Y. Zhang, Ch Liu and J. Jin, *Surface & Coating Technology* **202**, 4137–4144 (2008).

3. L. M. Chang, J. H. Liu and R. J. Zhang, *Materials and Corrosion*, No. 999, (Wiley, Weinheim, 2010).
4. C. Ernest Birchenall, *High Temperature Corrosion—NACE-6*, (National Association of Corrosion Engineers, Houston, 1982), pp. 3–7.
5. N. Birks, G. H. Meier and F. S. Pettit, *Introduction to the High-Temperature Oxidization*, 2nd ed, (Cambridge University Press, Cambridge, 2006).
6. J. M. West, *Basic Corrosion and Oxidation*, 1st ed, (Ellis Horwood Ltd., Chichester, 1980).
7. S. A. Bradford, *Fundamental of Corrosion in Gases, Corrosion*, vol. 13, (ASM, Materials Park, 2001), pp. 62–76.
8. J. R. Davis, *Heat-Resistant Materials*, (ASM International Handbook, Materials Park, 1999), p. 36.
9. M. A. Wahab, *Solid State Physics—Structure and Properties of Materials*, Chapter 6, 2nd edn. (Alpha Science International Ltd., Middlesex, 2005).
10. D. F. Susan and A. R. Marder, *Oxidation of Metals* **57**, 131–158 (2002).
11. D. F. Susan and A. R. Marder, *Oxidation of Metals* **57**, 159–180 (2002).
12. R. K. Saha, I. U. Haq, T. I. Khan and L. B. Glenesk, *Key Engineering Material* **442**, 187–194 (2010).
13. P. Baghery, M. Farzam, A. B. Mousavi and M. Hosseini, *Surface & Coatings Technology* **204**, 3804–3810 (2010).
14. L. Chen, L. Wang, Zh Zeng and J. Zhang, *Material Science and Engineering A* **434**, 319–325 (2006).
15. H. Gül, F. Kilic, S. Aslan, A. Alp and H. Akbulut, *Wear* **267**, 976–990 (2009).
16. C. L. Zeng, M. C. Li, G. Q. Liu and W. T. Wu, *Oxidation of Metals* **58**, 171–184 (2002).
17. M. A. Farrokhzad and T. I. Khan, *Key Engineering Materials* **510–511**, 32–42 (2012).
18. M. A. Farrokhzad, G. C. Saha, and T. I. Khan, *Surface and Coating Technology*. doi:[10.1016/j.surfcoat.2013.07.015](https://doi.org/10.1016/j.surfcoat.2013.07.015).
19. ASTM International, ASTM G16-95, *Standard Guide for Applying Statistics to Analysis of Corrosion Data* (ASTM International Ltd., West Conshohocken, PA, 2010). doi:[10.1520/G0016-95R10](https://doi.org/10.1520/G0016-95R10).
20. J. S. Milton and J. C. Arnold, *Introduction to Probability and Statistics*, 3rd ed, (McGraw-Hill, New York, 1995), pp. 391–398.
21. D. R. Gabe, *Principle of Metal Surface Treatment and Protection*, 2nd ed, (Pergamon, Oxford, 1978).
22. G. Parida, D. Chaira, M. Chopkar and A. Basu, *Surface and Coating Technology* **205**, 4871–4879 (2011).
23. B. Phillips, et al., *Journal of the American Ceramic Society* **46**, 579–583 (1963).
24. M. A. Rhamdhani, et al., *Metallurgical and Materials Transactions B* **40B**, 25–37 (2009).
25. K. P. Trumble and M. Rühle, *Acta Metallica Materialia* **39**, 1915–1924 (1991).
26. K. P. Lopes, et al., *Journal of Alloys and Compounds* **468**, 327–332 (2009).
27. A. Qiu et al., *Transactions of Nonferrous Metals Society of China*, vol. 21. (Nonferrous Metall Society of China Editorial Office, Changsha, 2011), pp. 1808–1816. <http://www.elsevier.com/journals/transactions-of-nonferrous-metals-society-of-china/1003-6326>.
28. D. Ortiz de Zarate, et al., *New Journal of Chemistry* **29**, 141–144 (2005).
29. G. M. Kale, *Metallurgical and Materials Transactions B* **29B**, 31–38 (1998).
30. W. Laqua and H. Schmalzried, *High Temperature Corrosion—NACE-6*, (National Association of Corrosion Engineers, Houston, 1982), pp. 110–114.
31. D. J. Taylor, P. F. Fleig, S. T. Schwab and R. A. Page, *Surface and Coating Technology* **120–121**, 465–469 (1999).